Chapter

Melt Treatment-Porosity Formation Relationship in Al-Si Cast Alloys

Dominique Gagnon, Agnes M. Samuel, Fawzy H. Samuel, Mohamed H. Abdelaziz and Herbert W. Doty

Abstract

The present study focuses on the porosity formation in three Al-Si cast alloys widely used in automotive industries viz. A319.0, A356.0, and A413.0 alloys under various conditions: stirring, degassing. Sr level, amount of grain refining, combined modification and grain refining, as well as hydrogen level. The solidification rate was the same for all alloys in terms of the mold used and its temperature. The microstructural investigations were carried out quantitatively using an optical microscope-image analyzer system scanning systematically over a polished sample area of 25 mm × 25 mm and qualitatively using an electron probe microanalzer equipped with EDS and WDS systems. The results were coupled with hardness measurements.

Keywords: aluminum alloys, modification, grain refining, degassing, oxides, porosity

1. Introduction

The presence of porosity in aluminum castings is inevitable to a certain extent. Porosity in aluminum-silicon castings occurs when dissolved hydrogen liquid metal is rejected out during solidification through the interdendritic regions to compensate for the shrinkage associated with the solidification caused by the change in the casting volume. Hydrogen is the only gas that dissolves to a large extent in molten aluminum, leading to the formation of porosity [1, 2]. Majority of the studies of porosity formation in aluminum alloys have been carried out on aluminum silicon cast alloys [3–6]. According to Bian et al. [7], porosity can be classified into two categories: (i) microporosity (1–10 mm). This type of porosity is mainly shrinkage due to lack of molten metal feeding which is normally observed in alloys with long freezing range (e.g. 319 and 356 alloys), and (ii) microporosity (<500 μm) distributed uniformly throughout the matrix and caused by the rejection of the dissolved hydrogen gas.

Beside the hydrogen, modification with Sr or grain refining using Al-Ti-B master alloys would influence the formation of porosity. The porosity formed in Sr-modified castings has been related to a number of parameters i.e. hydrogen level of the melt, feedability (long mushy zone), and changes in the mechanism of eutectic nucleation [8]. Porosity characteristics in Sr-treated alloys depend on the amount of Sr oxides formed during solidification. Also, the presence of aluminum

oxide films would result in the formation of large pores that are linked together. The end result can be explained in terms of the difference in eutectic solidification in unmodified and Sr-modified alloys [9, 10]. Dinnis et al. [11] examined the amount, distribution, and morphology of porosity in sand-cast plates of Sr-free and Sr-containing Al-(0–9 wr%) Si alloys. The authors found that no apparent differences in the amount, distribution, and morphology of porosity were observed between Sr-free and Sr-containing alloys with no Si (i.e. pure Al). However, Sr modification significantly changed the amount, distribution, and morphology of porosity in alloys with high Si content.

Influence of oxides on porosity formation in Sr-treated alloys was investigated by Samuel et al. [12] in 319 and 356 alloys. Their findings show that porosity formation is frequently associated with strontium oxides (particles or films), as well as β-Al_5FeSi phase platelets. The Al_2SrO_3 oxides are formed during melting by the high oxygen affinity of strontium. These oxides are difficult to be removed via degassing. Aluminum oxide films trapped in the molten metal result in the precipitation of coarser and deeper pores than those formed due to the strontium oxides [13].

According to Campbell and Tiryakioğlu [14], the beneficial effect of Sr as a modifying agent could be compromised by porosity development caused by the formation of oxide bifilms. The authors suggested an explanation in terms of the oxide population in the melt. A new multi-zone model is proposed by SkatTiedje et al. [15]. This model was developed by considering the effect of cooling rate on solidification and distribution of porosity in cast Al–Si alloys. The effect of Sr-modification on pore formation in reduced pressure and atmospheric conditions was studied by Miresmaeili et al. [16–18]. A new type of metallic cup with a riser was designed for use in a reduced pressure test as a mold. It was designed to improve directional solidification so that no macro shrinkage occurred in the test samples.

Another parameter to be considered is the presence of Fe-based intermetallics, in particular β-Al_5FeSi. Taylor et al. [19] investigated the role of iron in the formation of porosity in Al-Si-Cu-based casting alloys. Their analysis pointed to inadequacies in the existing theories regarding the role of iron and suggests that a new theory is required to understand the observed behavior. Effect of alloy composition on the stability of the β-AlFeSi phase and the role of the latter in porosity formation in 319 and 356 alloys was studied by Khalifa et al. [20]. The β-phase particles are potential sites for porosity formation regardless of the alloy composition and the type or size of the β particles. SrO and Al_2Si_2 Sr particles were observed to have contact with the β-AlFeSi platelets in the microstructure. Thus, with the addition of Sr, finer, better distributed pores appear in the microstructure. The alloy tensile properties are greatly improved by: (a) Sr addition in the range 200–400 ppm, (b) increasing the Mn/Fe ratio to 0.7, (c) addition of 0.08%Be, (d) addition of 0.08% Be+0.02% Sr [21–23].

The present study was undertaken to emphasize the role of melt treatment parameters (stirring, degassing, Sr-modification, grain refining, hydrogen content, intermetallics) as well as alloy composition on porosity formation in Al-(6–11 wr%Si) cast alloys and their impact on the alloy hardness. The initial alloys were unmodified and contained 0.0075%Ti and less than 0.2%Fe.

2. Experimental procedure

Table 1 lists the chemical composition of the as received ingots. The ingots of each alloy were cut, cleaned and melted in an electrical heated furnace using 6 kg SiC crucibles. The melting temperature was about 750°C ± 5 °C. Degassing was

Alloy	Cu	Mg	Mn	Si	Fe	Sr	Ti	B
A319.0	3.112	0.0071	0.0005	5.59	0.170	0.0000	0.0105	0.0004
A356.0	0.060	0.314	0.0005	6.21	0.099	0.0001	0.0002	0.0002
A413.0	11.17	0.046	0.218	11.17	0.204	0.0000	0.0652	0.0003

Table 1.
Chemical composition of the as-received alloys (wt.%).

carried out using a perforated graphite impeller turning at 135 rpm using pure Ar gas (0.492 cubic meter/hr) for about 30–40 minutes. The same impeller was also used as stirrer without gas. Strontium was added in the form of Al-10%Sr master alloy (waffles) whereas grain refiner was introduced as Al-5%Ti-15B master alloy in the form of short rods. It should be mentioned here that the manufacturing of the grain refiner produces Al_2O_3 which will increase in the amount of porosity. For this reason, the grain refiner in this study was added in the form of short rods (cold rolled) to minimize the presence of such oxides.

Due to the high affinity of Sr to react with oxygen to form SrO oxides, Sr was added during the last 10 minutes of degassing. As for varying the hydrogen level, small pieces of raw potato were added at the end of degassing, (in this case, Sr was not used) followed by AlScan™ measurement. In addition, reduced pressure test (RPT) samplings were taken from the melts. **Figure 1** shows examples of RPT samples sectioned in half to examine the porosity observed under different melt conditions. In all cases, samples for chemical analysis were also obtained from each melt prior to pouring.

Following melt treatment, the molten metal was poured in L-shaped metallic molds (75 mm × 35 mm × 30 mm). The molds were coated with fine grained boron nitride and were preheated at 450°C **Figure 2**. **Table 2** summarizes the sample codes and their melt treatment whereas **Table 3** shows complete analysis of A356.0 alloy as an example.

Samples for metallographic examination were sectioned from the middle of the cast bars (25 mm × 25 mm) and polished following standard procedures [24]. Porosity characteristics were evaluated using a Clemex image analyzer in conjunction with an optical microscope. Measurements were carried out at 100× as shown in **Figure 3**. For each sample at least 100 fields were scanned to enhance the accuracy of measurements. Selected samples were examined using an electron probe microanalyzer (EPMA) equipped with EDS and WDS systems, operating at 20 kV.

In order to quantify the effect of melt treatment parameters, hardness measuremnts were carried out on the sample surface shown in **Figure 2** using Brinell hardness testing machine using a 10 mm diameter steel ball and 500 kgf force. For each condition, an average of 8 readings was reported. The samples of A319.0

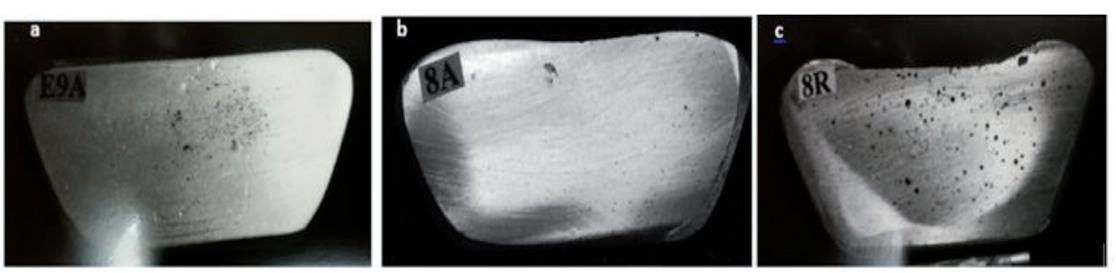

Figure 1.
RPT test taken from: (a) as received alloy, (b) after degassing, (c) 0.25 ml/100 g H_2.

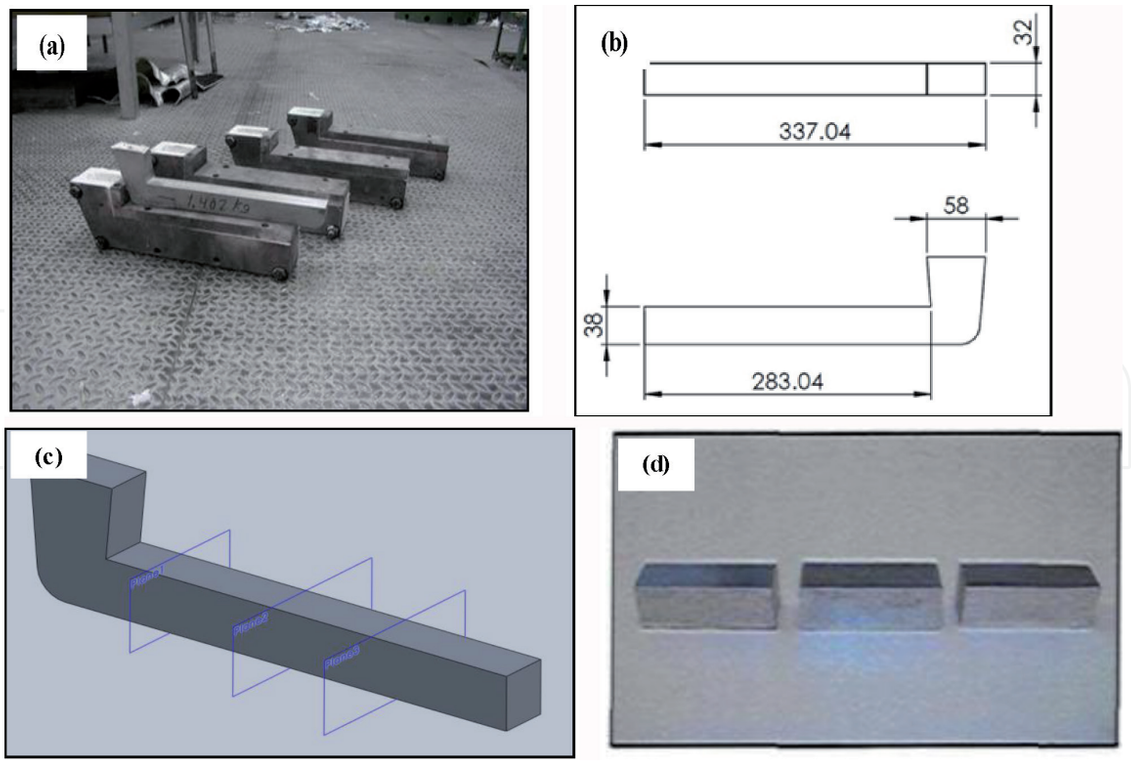

Figure 2.
L-Shape castings: (a) L-shape mold, (b) geometry of the L-shape casting, (c) cutting sequence of L-shaped casting to produce smaller rectangular bars, and (d) hardness test bars.

Metallurgical parameter	A319.0	A356.0	A413.0
Without degassing	A1	B1	C1
After degassing	A2	B2	C2
WithTiB_2 (0.11% Ti)	A3	B3	D3
With Sr (0.02%)	A4	B4	D4
With TiB_2 (0.11% Ti) and Sr (0.02%)	A5	B5	D5
H2 (0.15 ml/100 g)	A6	B6	D6
H2 (0.15 ml/100 g)	A7	B7	D7
With TiB_2 (0.11% Ti)	A8	B8	D8
With TiB_2 (0.22% Ti) and Sr (0.02%)	A9	B9	D9

Table 2.
Codes of the used alloy s and their melt treatment.

alloy were solution heat treated at 510°C for 8 h followed by water quenching. The samples thereafter were aged at various temperatures for 5 h followed by air cooling.

3. Results and discussion

3.1 Grain size

Selected samples from three levels of grain refining were used for macrostructure analysis. The polished samples were etched in a solution composed of (66% HNO_3, 33% HCl, 1% HF) and results are listed in **Table 4**. It is evident that with the increase in the amount of the added TiB_2 there is a significant decrease in the alloy

Code	Element (wt%)										
	Si	**Fe**	**Cu**	**Mn**	**Mg**	**Cr**	**Ti**	**B***	**Sr**	**H_2**	**Al**
B1	6.24	0.0993	0.0574	0.0005	0.3137	0.0004	**0.0002**	<0.0002	**0.0001**	degassed	93.3
B3	6.21	0.0991	0.0597	<0.0005	0.3143	<0.0005	**0.1075**	<0.0002	**0.0001**	degassed	93.2
B3	6.29	0.0927	0.0067	<0.0005	0.3171	<0.0005	**0.1127**	<0.0002	**0.0001**	degassed	93.1
B5	6.16	0.0943	0.0032	<0.0005	0.3149	<0.0005	**0.1082**	<0.0002	**0.0159**	degassed	93.3
B5	6.09	0.0925	0.0066	<0.0005	0.3121	<0.0005	**0.1122**	<0.0002	**0.0193**	degassed	93.3
B6	6.17	0.1781	0.2087	0.0107	0.2854	0.0007	**0.2104**	0.0360	**0.003**	degassed	92.6
B7	5.96	0.1596	0.1992	0.0101	0.2716	<0.0005	**0.2307**	0.0360	**0.0172**	degassed	92.8
B8	6.10	0.0990	0.1124	<0.0005	0.3116	<0.0005	**0.1094**	<0.0002	**0.0002**	~0.15 ml/100 g	93.2
B9	6.18	0.1052	0.0887	0.0011	0.3102	0.0007	**0.1117**	<0.0002	**0.0001**	~0.25 ml/100 g	93.1

**B was not determined.*

Table 3.
Actual chemical composition of A356.0 alloy melts prepared.

grain size, reaching about 80% when the concentration of grain refiner is about 0.2%Ti. **Figure 4** reveals the significant reduction in the grain size of the A413.0 alloy refined with 0.22%Ti. EPMA examination indicated that the initial Al-Ti-B master alloy was decomposed into TiB_2 (in the form of ultra-fine dispersed particles

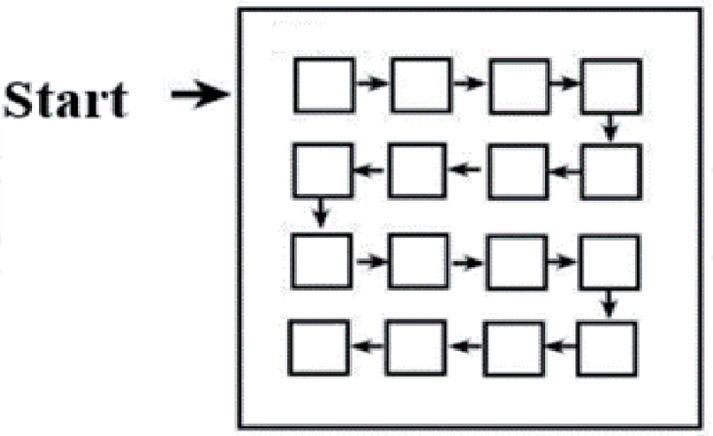

Figure 3.
Schematic distribution of the examined fields.

Code	Grains size (μm)	SD (μm)	%Refining
A1	678	29	base
A3	544	248	20
A6	214	54	68
B1	811	178	base
B3	692	293	15
B6	229	78	71
D1	2466	386	base
D3	2156	269	12
D6	475	97	80

Table 4.
Average grain size of the three alloys used.

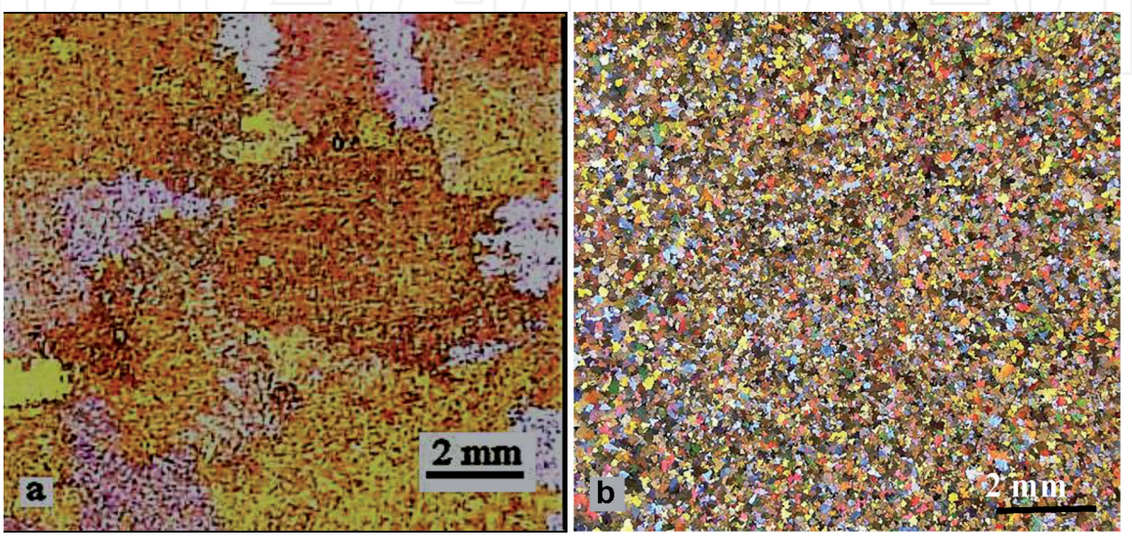

Figure 4.
Reduction in the grain size of the A413.0 alloy: (a) 0.007%Ti, (b) 0.22%Ti.

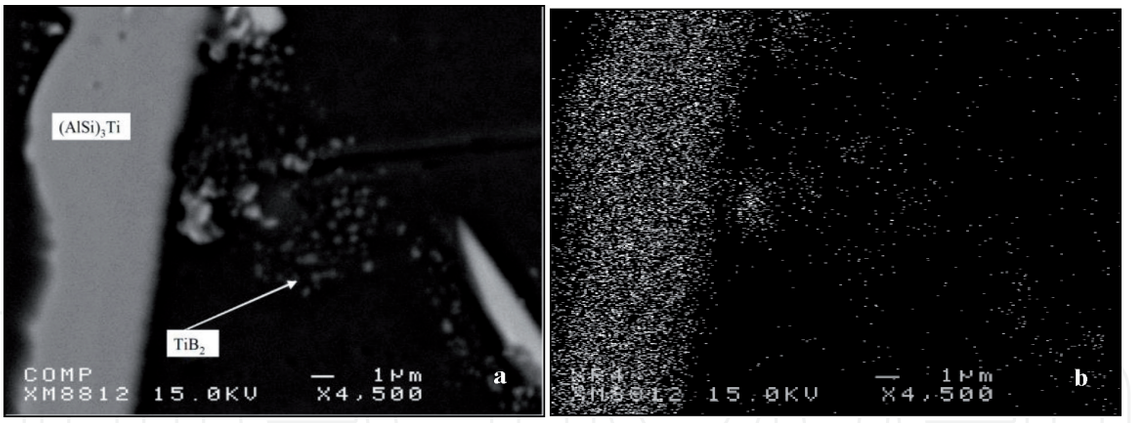

Figure 5.
Decomposition of the added Al-5%Ti-1%B master alloy: (a) backscattered electron image, (b) X-ray image of Ti distribution.

(50–100 nm) causing the observed refining) and platelets of $(AlSi)_3Ti$ within the α-aluminum as demonstrated in **Figure 5** [25, 26].

3.2 Porosity

It is deemed important to present the solidification curves (0.8°C/s) of the three used alloys in order to arrive at a clear understanding of the parameters that control the porosity characteristics. These curves are shown in **Figure 6**.

It is well established that porosity is formed due to dissolved hydrogen in the liquid metal, shrinkage during solidification process, and oxide films. Severity of porosity depends on the amount of these three parameters [1–3]. **Tables 5–7** present the measurements of the porosity characteristics as a function of the applied melt treatment. Degassing for a sufficient amount of time would lead to reduction in the dissolved hydrogen in the liquid metal as well as removal of most of inclusions and oxide films [14–18]. Thus all alloy melts were degassed prior to casting except for the hydrogen–containing alloys (coded 6 and 7) where degassing was done prior to introduction of H_2. It is inferred from these tables that hydrogen results in precipitation of large pores leading to a relatively high percentage of porosity with low pore density. Although Sr was added only 10 minutes before the end of degassing, however, the SrO formed during this period was enough to increase the amount of porosity but not as high as that caused by H_2.

The combined effect of oxides associated with the manufacturing of the grain refiner (mainly Al_2O_3) along with SrO contributed to the increase in the amount of porosity. It is noticed that the porosity in the A413.0 alloy is relatively less than in the other two alloys which may suggest that as-received alloy was previously degassed using chlorine, as inferred from its low Mg content (see **Table 1**). Also, it is should be taken into consideration that A413.0 alloy has a short freezing range compared to A319.0 and A356.0 alloys, see **Figure 5**. The average aspect ratio of the samples without degassing falls in the range of 2.0–2.3. After gassing, the average values of the aspect ratio lie in the range 1.2–1.32 indicating that the precipitated pores are more-or-less of spherical shape. However, in all cases, degassing with Ar could reduce the porosity by about 90%.

Figure 7 presents a comparison of average pore area and porosity percentage parameters for the three used alloys, highlighting the effect of oxides (SrO, Al_2O_3 films and/or bifilms), and the effect of hydrogen content. As can be seen there is a direct proportionality between the two parameters, associated with low pore density indicating porosity agglomeration which would lead to poor mechanical properties.

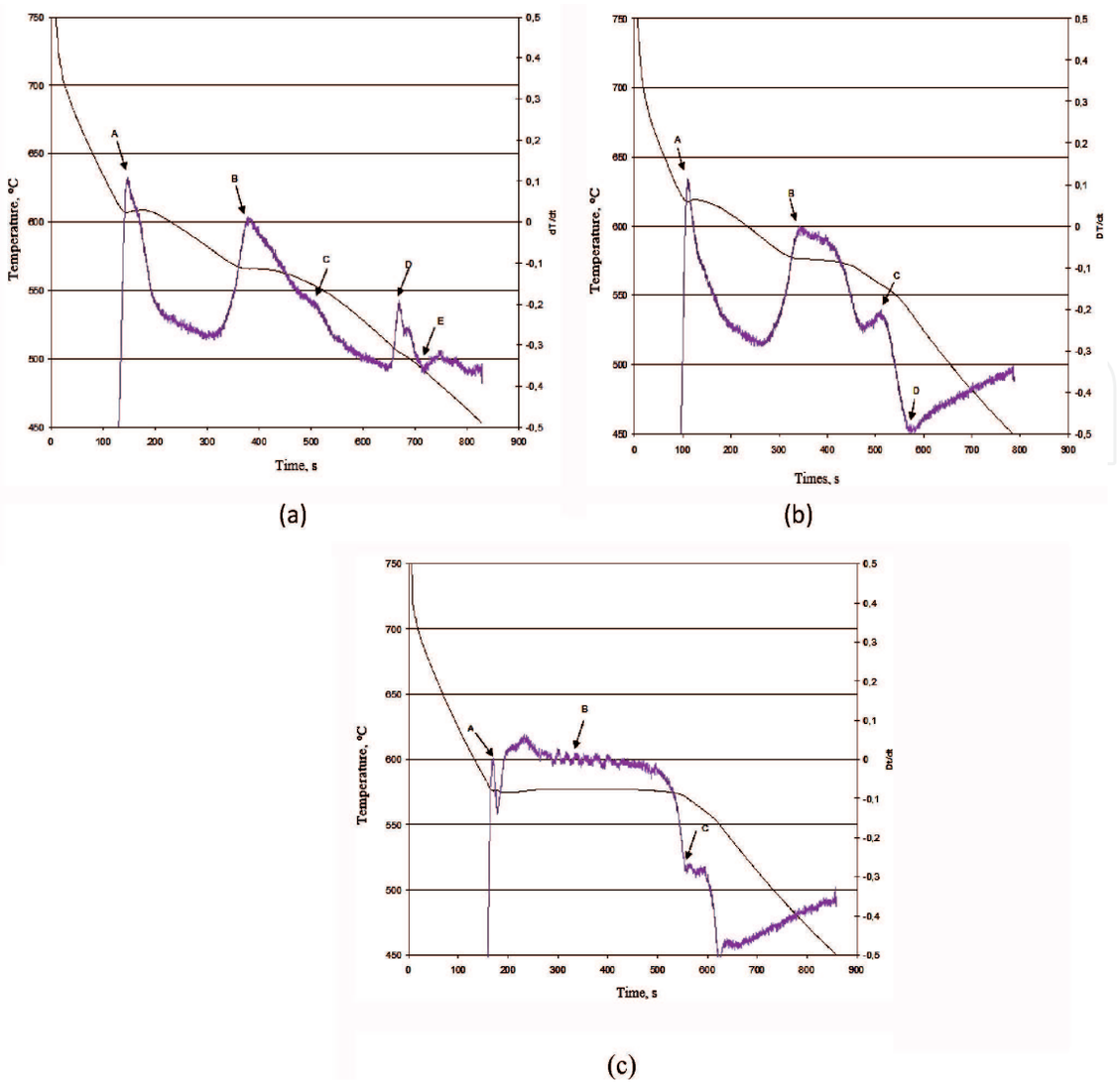

Figure 6.
Solidification curves and their first derivatives obtained for: (a) A319.0, and (b) A356.0, (c) A413.0 alloys.

Code	Average pore area (μm²)		Average pore length (μm)		Aspect ratio		Density (pores/μm²)	Ave area percentage (%)	
	Ave.	SD	Ave.	SD	Ave.	SD	—	Ave.	SD
A1	682	231	41	16	2.3	0.70	5.86	0.356	0.207
A2	99	123	12	08	1.63	0.69	2.80	0.029	0.018
A3	129	61	25	17	1.53	0.76	5.89	0.125	0.108
A4	844	119	30	17	1.60	0.56	2.78	0.780	0.041
A5	762	371	75	25	1.86	0.69	9.89	0.488	0.135
A6	975	325	40	12	1.32	0.62	6.64	1.845	0.317
A7	1505	368	106	23	1.29	0.53	5.61	2.414	0.039
A8	465	100	36	21	1.78	0.61	9.66	0.418	0.215
A9	1023	448	43	14	1.78	0.68	7.05	0.843	0.267

Table 5.
Characteristics of porosity in A319.0 alloy.

In general, the formation of pores is governed by the relation: $\Delta P = 2\sigma/r$, where σ is the surface tension, and ΔP is the critical pressure needed to create a nuclei of radius r [27]. Thus, introducing a high level of H_2 in the liquid

Code	Average pore area (μm^2)		Average pore length (μm)		Aspect ratio		Density (pores/μm^2)	Ave. area percentage (%)	
	Ave.	SD	Ave.	SD	Ave.	SD	—	Ave.	SD
B1	201	72	74	43	2.01	0.52	3.22	0.570	0.455
B2	59	81	14	11	1.83	0.43	2.08	0.026	0.049
B3	178	325	19	19	1.67	0.84	2.58	0.168	0.052
B4	1113	208	48	24	1.35	0.65	1.30	0.424	0.078
B5	1014	129	123	46	1.24	0.85	4.61	0.604	0.170
B6	1230	612	54	22	1.29	0.39	1.17	1.451	0.283
B7	1893	189	98	34	1.15	0.40	2.89	1.952	0.196
B8	484	274	26	11	1.75	0.68	2.75	0.388	0.060
B9	1488	452	29.76	24.77	1.70	0.69	5.78	0.556	0.126

Table 6.
Characteristics of porosity in A356.0 alloy.

Code	Average pore area (μm^2)		Average pore length (μm)		Aspect ratio		Density (pores/μm^2)	Ave area percentage (%)	
	Ave.	SD	Ave.	SD	Ave		Ave.	Ave	SD
D1	157	244.9	15	08	2.12	0.38	0.17	0. 20	0.004
D2	82	71.44	15	09	1.76	0.62	0.19	0.01	0.002
D3	454	462	30	14	1.56	0.65	0.83	0.134	0.038
D4	832	236	40	16	1.56	0.55	2.19	0.357	0.222
D5	935	296	61	21	1.87	0.60	1.14	0.592	0.148
D6	1490	341	17	21	1.31	0.53	1.72	0.643	0.157
D7	1840	802	46	21	1.29	0.41	2.08	0.857	0.186
D8	785	122	19	07	1.67	0.75	5.97	0.305	0.066
D9	965	181	35	05	1.70	0.66	6.58	0.552	0.182

Table 7.
Characteristics of porosity in A413.0 alloy.

aluminum would increase ΔP, decreasing r, and hence increasing the porosity percentage. **Figure 8(a)** shows an example of the pore shape observed in gassed A413.0 alloy (coded D6) where the pore is almost round. **Figure 8(b)** represents a pore caused by the shrinkage of the casting on going from liquid to solid state. Due to volume change associated with this process, the final casting shrinks by about 7%, which is accommodated within the final cast in the form of irregular pores passing through the interdendritic structure (**Figure 8(b)**). In certain cases, the gas pore could later on change into a shrinkage pore as seen in **Figure 8(c)**, depending on the level of dissolved gas.

Formation of oxide films during the course of melting due to insufficient degassing could lead to formation of massive pores as in the case of Sr-modified alloys where Sr was exposed to the outer atmosphere for a long period of time, as exemplified in **Figure 8(d)**. Li et al. [28] determined the nature of this oxide as $Al_{2.3}SrO_{3.3}$ using WDS analysis. Another type of oxide films associated with the pores is displayed in **Figure 8(e)** where the molten metal was partially stirred. According to Mohanty et al. [29] this type of oxide can act as nucleation sites for pore formation

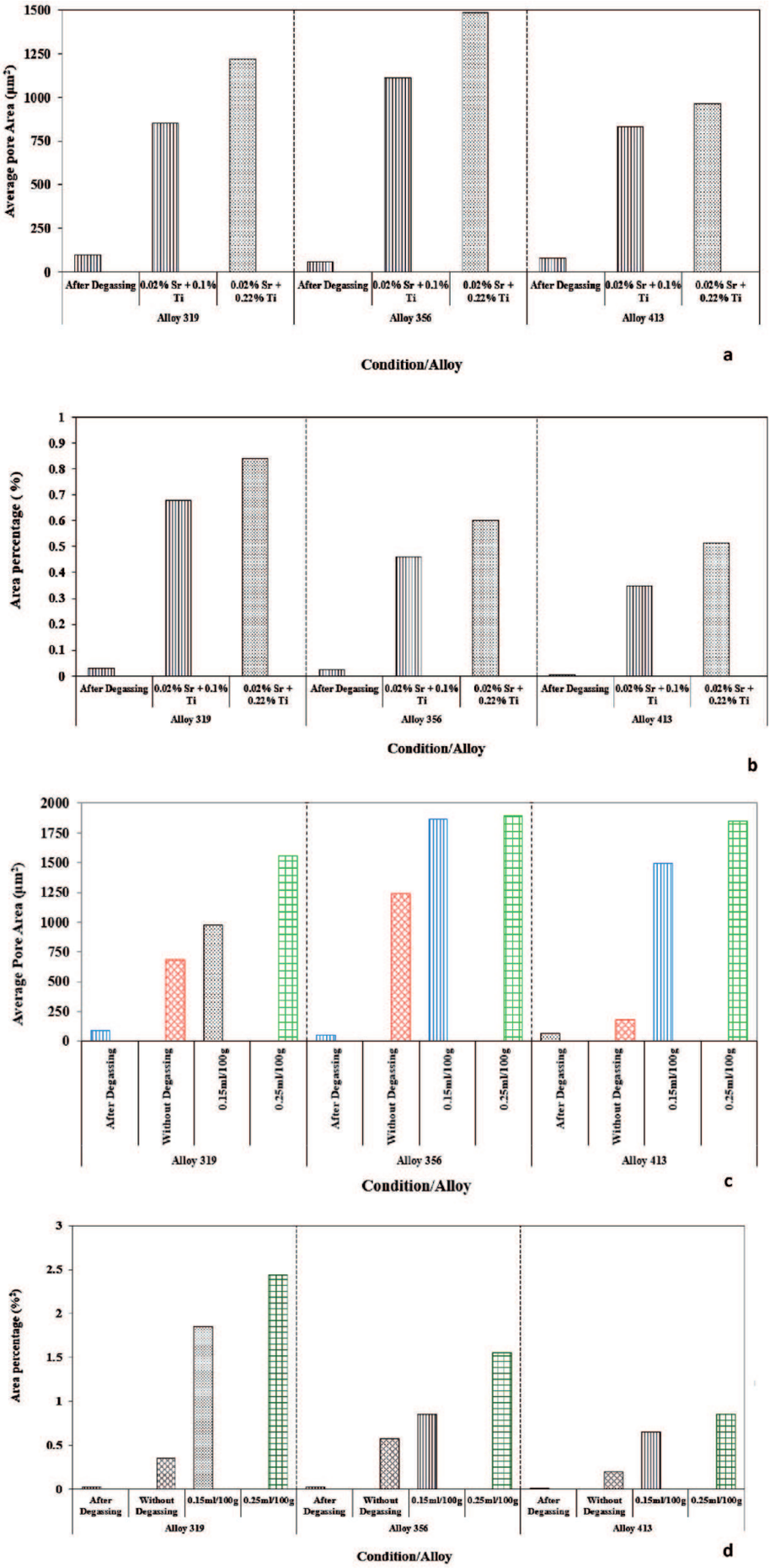

Figure 7.
Comparison of oxides and hydrogen level on the alloy pore size and porosity percentage: (a, b) effect of oxides as a function of the total amount of added Sr and grain refiner, (c, d) effect of hydrogen level.

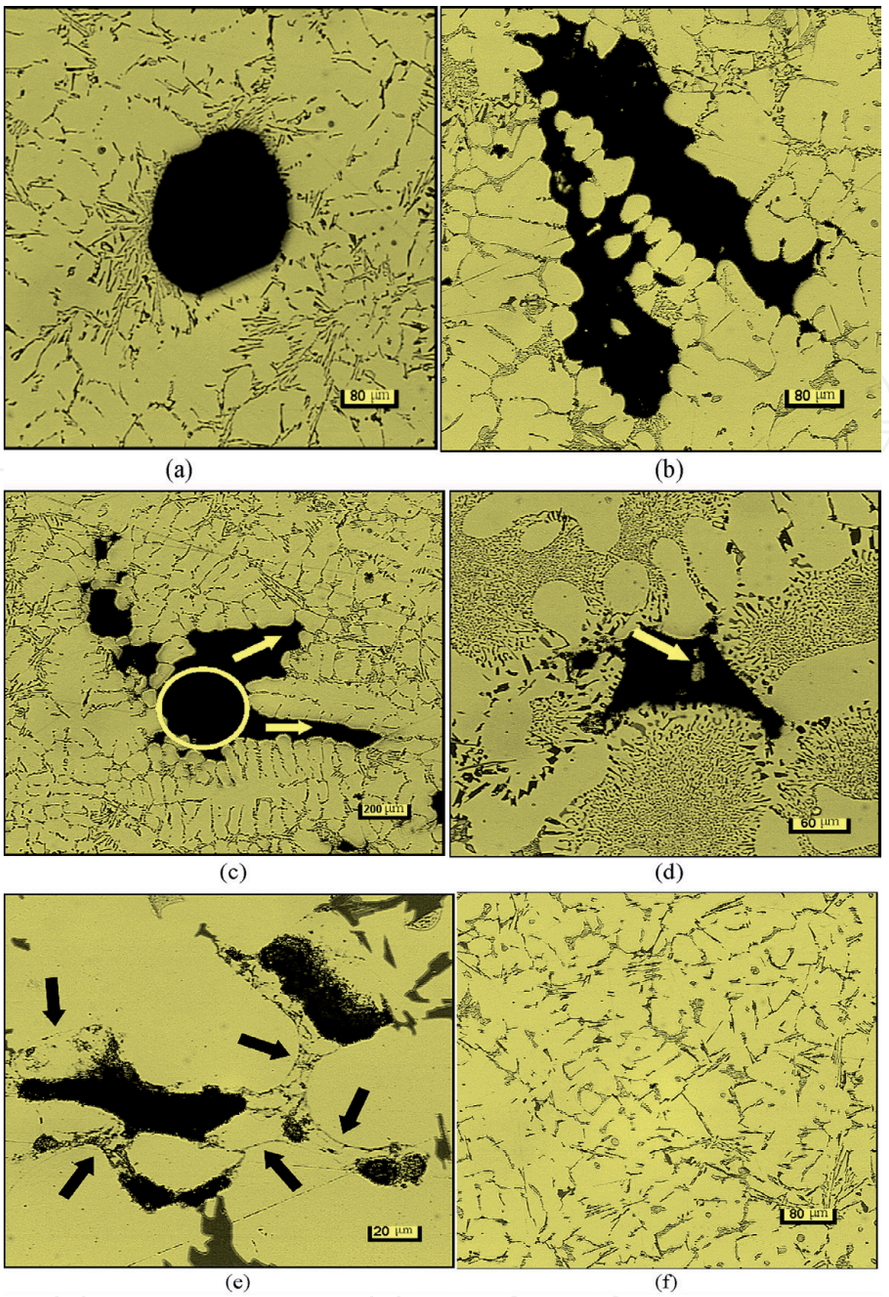

Figure 8.
Effect of melt treatment on the pore morphology in A413 alloy: (a) D6, (b) D9, (c) D7, (d) D3, (e) D1, (f) D2.

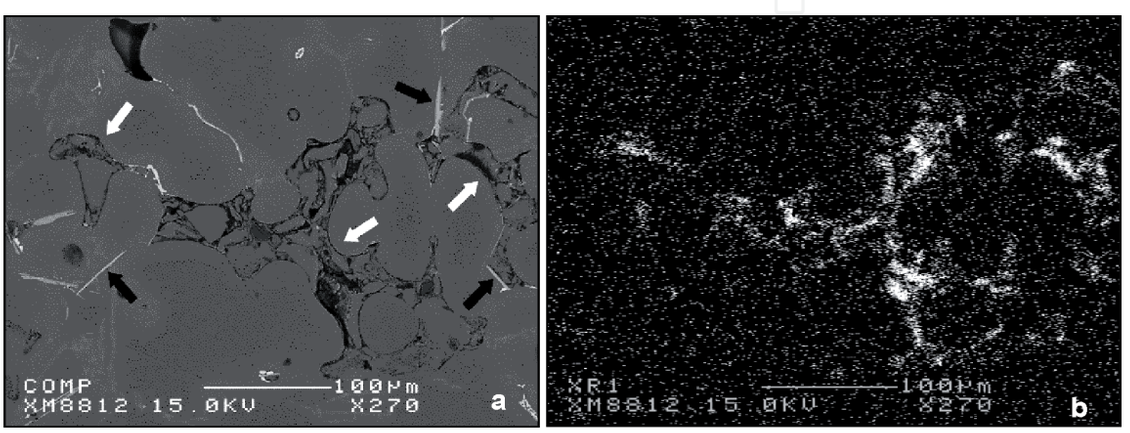

Figure 9.
(a) Backscattered electron image of D9 alloy, (b) X-ray map showning distribution of O_2 in (a).

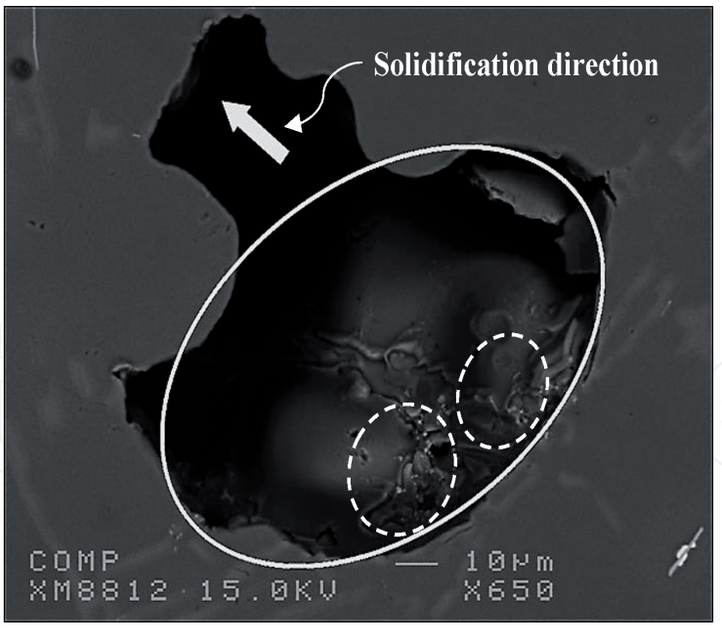

Figure 10.
Backscattered electron image revealing a massive pore composed of gas and shrinkage.

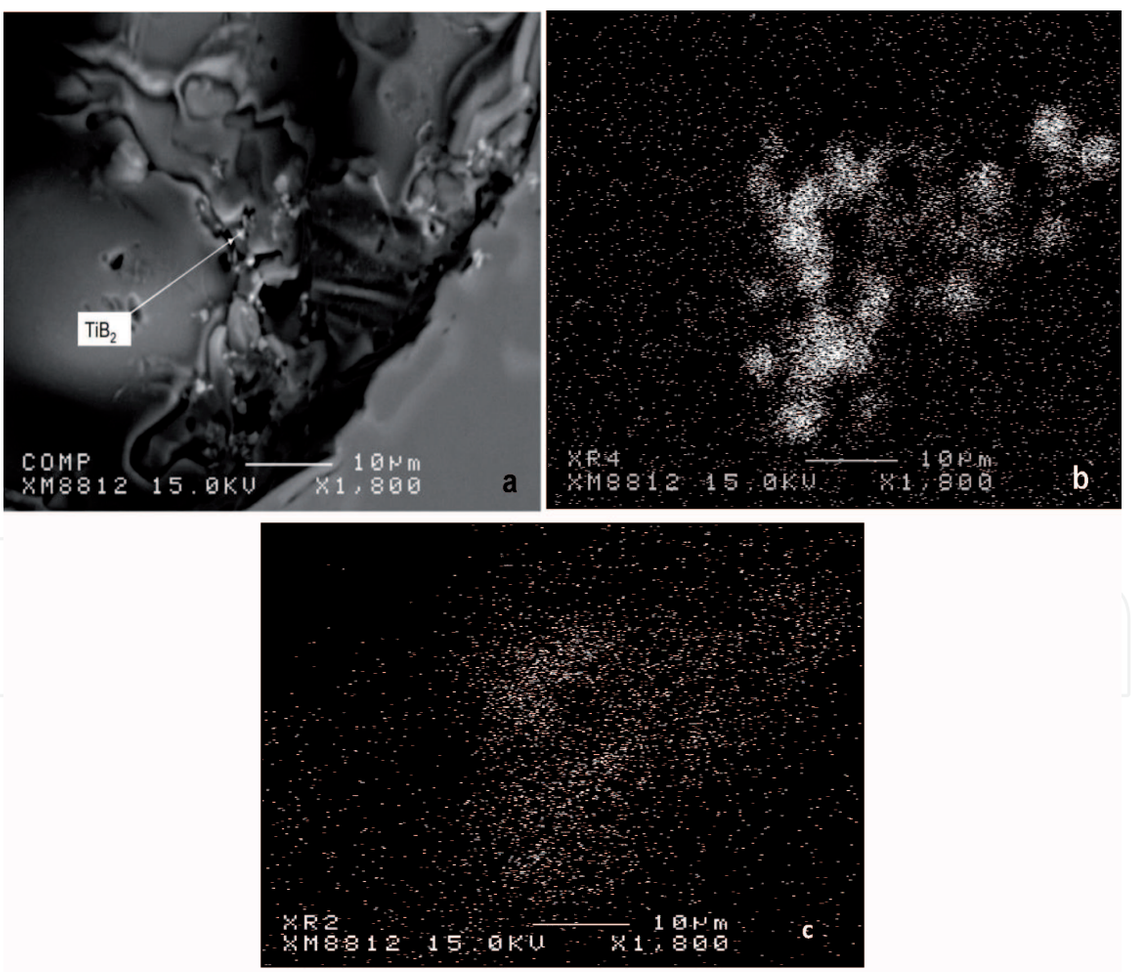

Figure 11.
(a) High magnification backscattered electron image of the white area in ***Figure 7*** *(broken line), (b, c) X-ray maps revealing the distribution of Ti and B, respectively, in (a).*

as shown by the black arrows in **Figure 7(e)**. **Figure 8(f)** exhibits the microstructure of a well degassed sample. **Figure 9(a)** is a backscattered electron image of D9 alloy (high Ti content) revealing the oxide films or bifilms [14] associated with the

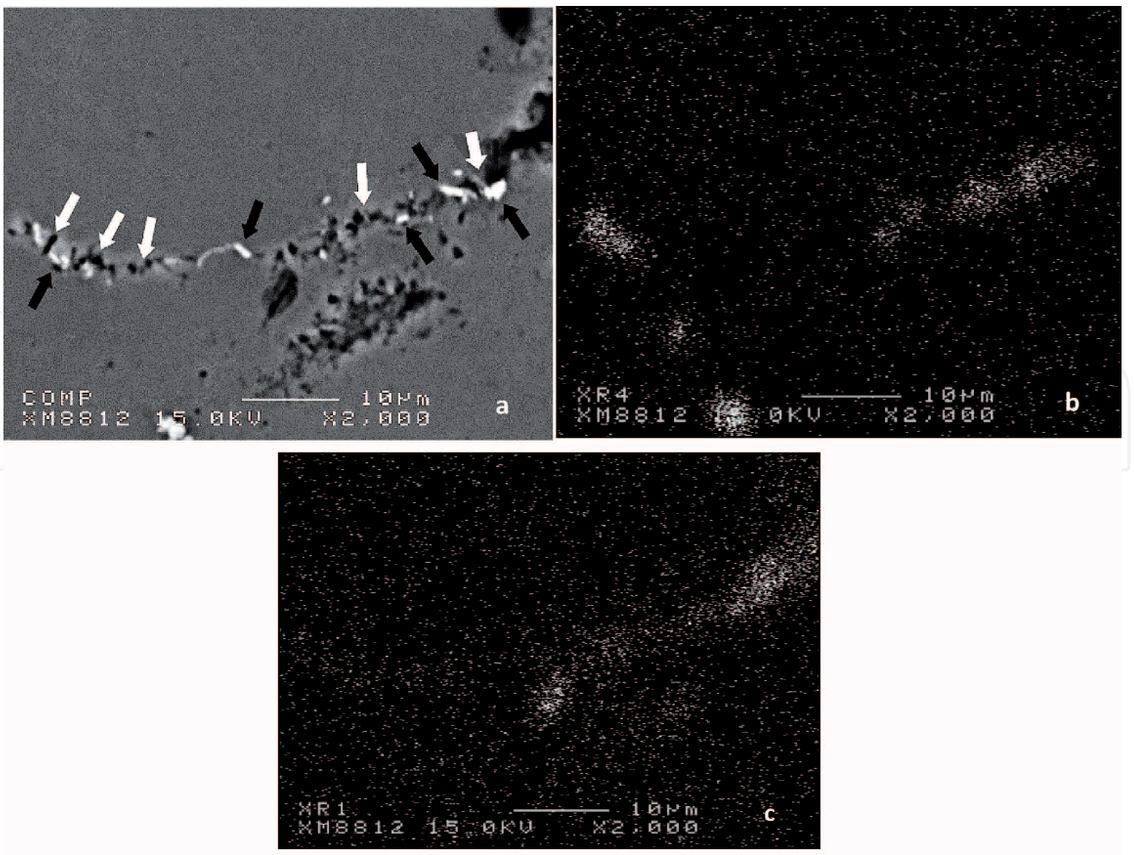

Figure 12.
(a) Backscattered electron image of TiB_2 particles mixed with SrO particles/films in D9 alloy, (b and c) X-ray maps of Ti and O_2, respectively in (a). The bright spots are fragments of SrO films.

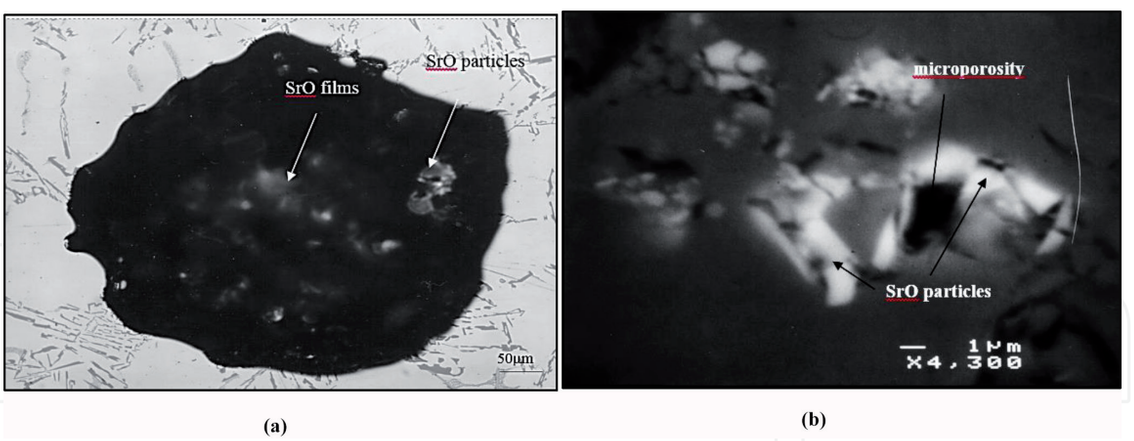

Figure 13.
(a) SrO films and particles observed within a pore in 319 alloy; (b) backscattered electron image showing SrO particles situated inside the pore [30, 31].

manufacturing of the Al-Ti-B master alloy (white arrows) and present in the sample due to insufficient degassing or mechanical stirring. The black arrows highlights the presence of $(Al.Si)_3Ti$ platelets in the vicinity of the oxide films.

Figure 10 is a backscattered electron image of **Figure 8(c)** displaying the change in the nature of the precipitated pore from round (due to H_2) into irregular (shrinkage-white arrow) pore during the coarse of solidification leading to the formation of a massive pore in D9 that contains high amounts of Ti and Sr. The presence of utlra fine particles was noticed within the gas pore (white broken lines) in **Figure 10**. A high magnification image of this part is displayed in **Figure 11(a)** revealing the presence of

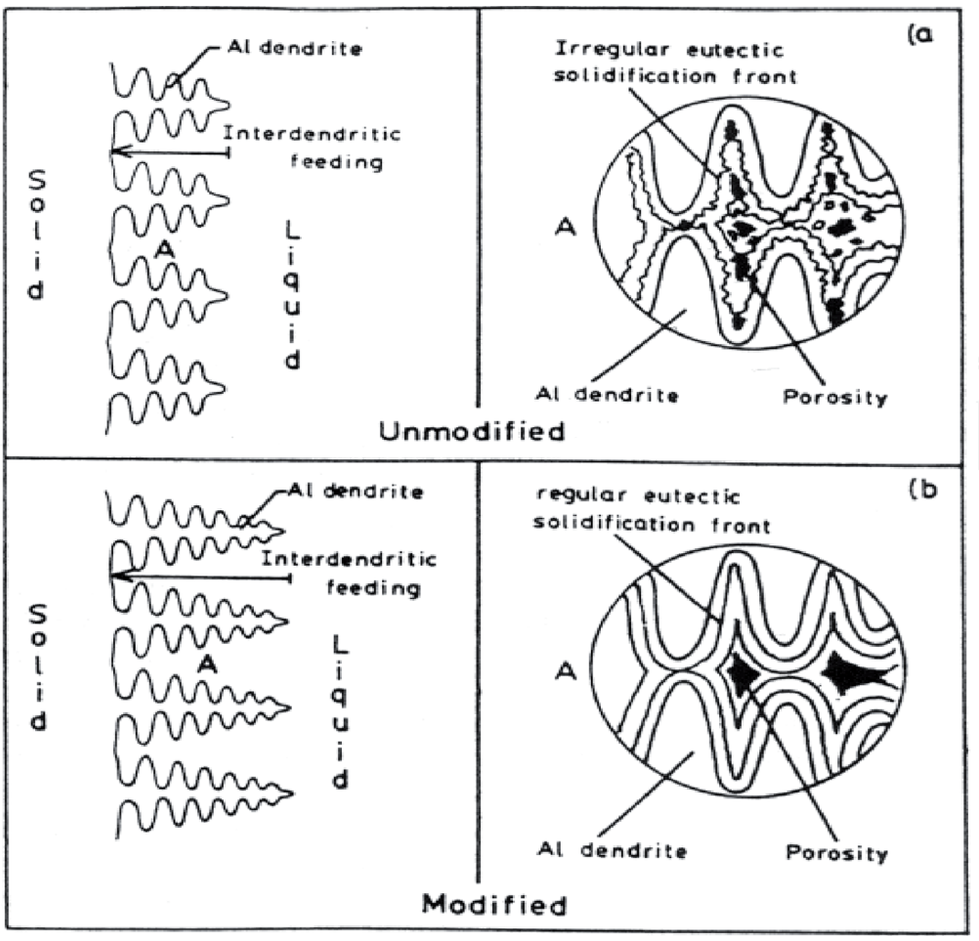

Figure 14.
The formation of porosity in: (a) unmodified alloys, (b) Sr-modified alloys [32].

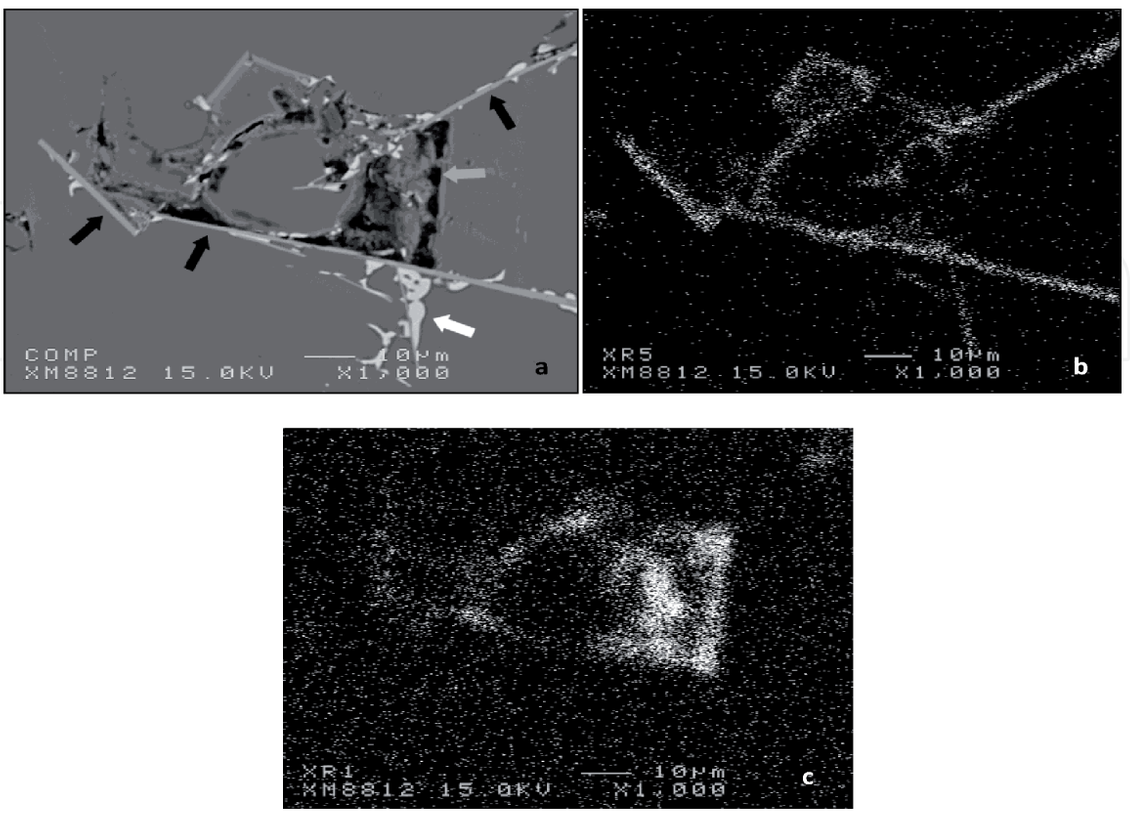

Figure 15.
(a) Backscattered electron image of oxide films mixed with β-Al_5FeSi platelets in D9 alloy, (b and c) X-ray maps of Fe and O_2, respectively in (a).

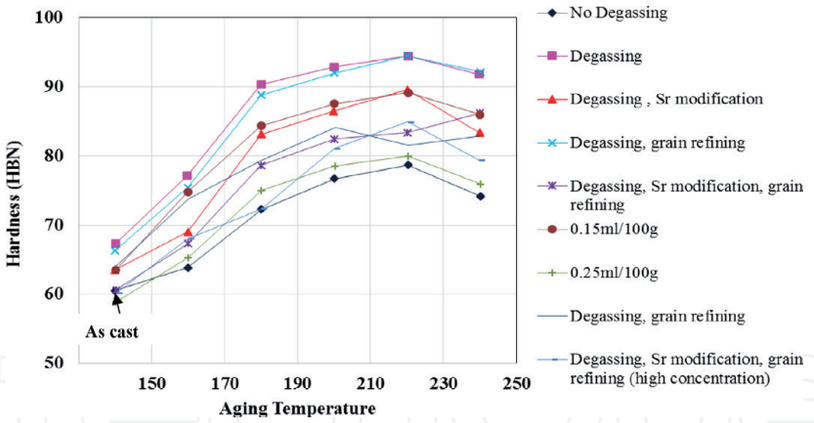

Figure 16.
Variation of the hardness of A319.0 alloy as a function of aging temperature and the applied melt treatment.

TiB_2 particles withing the gas pore as idendified by the X-ray electron maps presented in **Figure 11(b)** and **(c)**. As can be seen the X-ray map of Ti is well defined in the form of round spots whereas that of B is almost covering the entire area.

Figure 12 reveals another feature observed in D9 alloy the co-existence of TiB_2 (white arrows) alongwith SrO oxide films (or bifilms - bright spots) resulting in the formation of microporosity (black arrows). In earlier studies [30, 31], the authors' group showed the presence of microporosity in Sr-modified A319.0 alloy surrounded by SrO oxides as demonstrated in **Figure 13**.

The above-mentioned discussion contradicts the theory proposed by Argo and Gruzleski [32], who suggested that in unmodified alloys, the eutectic is characterized by its irregular solid/liquid interface, leading to entrapping of small pockets of liquid between advancing solidification fronts, causing the formation of microporosity, as shown in **Figure 14**. In Sr-modified alloys rather, a regular or planar interface results in widely dispersed larger porosity.

Figure 15(a) illustrates another source of porosity formation in D9 alloy. In this case, both the oxide films (gray arrows) and β-Al5FeSi platelets (black arrows) participated in the nucleation of irrgular pores [33–36]. Apparently the β-Al5FeSi platelets also act as a barrier blocking the propagation of the pore through the matrix. **Figure 15(b)** and **(c)** confirm the presence of the oxide films interacted with the β-Al5FeSi platelets. The white arrow in **Figure 15(a)** indicates the presence of a coarse Al_2Cu phase particle with no pores associated with it.

Figure 16 illustrates the variation in the hardness of the A319.0 alloy as a function of aging temperature and applied melt treatment. As can be seen, regardless of the applied treatment, all curves follow the same pattern since they are controlled by the precipitation of Al_2Cu phase particles. Apparently, the age hardening mechanism is completely independent of the melt treatment. In contrast, the hardness level revealed a clear response to the melt treatment used. When the alloy was not degassed, the hardness values were the lowest compared to other treatments, whereas the situation is inversed after proper degassing. Due to oxides associated with the grain refiner as well as the presence of SrO, the hardness dropped markedly. Increasing the hydrogen content to 0.25 ml/100 g (and hence a significant amount of porosity) led to hardness levels close to those obtained for mechanically stirred alloy (i.e., with no degassing).

4. Conclusions

Based on the results documented in the present work, the following conclusions may be drawn:

1. The use of the proper amount of grain refiner reduces the grain size of the as received alloy by about 80%. This refinement is mainly due to the large number of TiB_2 particles (50–100 nm).

2. Proper degassing can reduce the amount of porosity by about 90%.

3. Oxide films (or bifilms) either as a part of the added grain refiner, or due to oxidation of Sr, or both, would result in a significant increase in the percentage of porosity, thereby deteriorating the alloy strength, regardless of the applied aging treatment.

4. With respect to porosity formation, another parameter to consider is the alloy freezing range.

5. Although increasing the hydrogen level would lead to precipitation of round pores instead of the irregular shrinkage ones, such pores could markedly reduce the alloy strength to the level corresponding to the mechanically stirred alloy in the molten state.

6. Not all intermetallics contribute to the porosity formation except for the β-Al_5FeSi phase due to its precipitation in the form of intersecting platelets.

7. Age hardening behavior/pattern is governed by the hardening precipitates i.e., Al_2Cu and Mg_2Si, whereas the hardening level is a direct function of the applied melt treatment.

Author details

Dominique Gagnon[1], Agnes M. Samuel[1], Fawzy H. Samuel[1*], Mohamed H. Abdelaziz[2*] and Herbert W. Doty[3]

1 Département des Sciences Appliquées, Université du Québec à Chicoutimi, Chicoutimi, Canada

2 Département PEC, Universite' Française d'E' gypte, Ville Shorouk, Le Caire, Egypt

3 General Motors Materials Engineering, 823 Joslyn Ave, Pontiac, MI 48340, USA

*Address all correspondence to: fhsamuel@uqac.ca and mohamed.abdelaziz@ufe.edu.eg

References

[1] Li XZ, Bian XF. Behavior of Hydrogen in Superheated Aluminum and its Alloys Melt. Materials Science Forum. 2000;**331-337**:209-214

[2] Anyalebechi PN. Hydrogen-induced gas porosity formation in Al–4.5 wt% Cu–1.4 wt% Mg alloy. Journal of Materials Science. 2013;**48**:5342-5353

[3] Jang Y, Jeong Y, Yoon C, Kim S. Fatigue life prediction for porosity-containing cast 319-T7 aluminum alloy. Metallurgical and Materials Transactions A. 2009;**40A**:1090

[4] Roy NR, Samuel AM, Samuel FH. Porosity formation in AI-9 Wt pct Si-3 Wt pct Cu alloy systems: Metallographic observations. Metallurgical and Materials Transactions A. 1996;**27**(2):415-429

[5] Roy NR, Zhang L, Louchez PR, Samuel FH. Porosity formation in Al-9 wt% Si3 wt% Cu-X alloy systems: Measurements of porosity. Journal of Materials Science. 1996;**31**(5):1243-1254

[6] A.M Samuel, F.H. Samuel and N.R. Roy, Porosity formation in Al-Si-Cu alloys: Role of intermetallics, in *Proceedings of the Light Metals Symposium, 35th Annual Conference of Metallurgists of CIM, Montreal, Quebec,* August *25-29, 1996*, p. 269.

[7] Bian XF, Zhang ZH, Liu XF. Effect of Strontium Modification on Hydrogen Content and Porosity Shape of Al-Si Alloys. Materials Science Forum. 2000;**331-337**:361-366

[8] Liu L, Samuel AM, Samuel FH, Doty HW, Valtierra S. Influence of oxides on porosity formation in Sr-treated Al-Si casting alloys. Journal of Materials Science. 2003;**38**:1255-1267

[9] Dahle AK, Nogita K, McDonald SD, Dinnis C, Lu L. Eutectic development and microstructure development in Al-Si alloys. Materials Science and Engineering A. December 2005;**413-414**(15):243-248

[10] F.H. Samuel, A.M. Samuel, H.W. Doty, S. Valtierra, On Porosity Formation in Al–Si–Cu Cast Alloys, Light Metals, 2017, pp. 243-255.

[11] C. M. Dinnis, M. O. Otte, A. K. Dahle, J. A. Taylor, The influence of strontium on porosity formation in Al-Si alloys, Metallurgical and Materials Transactions A, Vol. 35A (11), 2004, pp. 17-30.

[12] Samuel AM, Doty HW, Valtierra S, Samuel FH. Influence of Oxides on Porosity Formation in Sr-Treated Alloys. International Journal of Metalcasting. 2017;**11**:729-742

[13] Ye H. An overview of the development of Al-Si-Alloy based material for engine applications. Journal of Materials Engineering and Performance. 2003;**12**:288-297

[14] Campbell J, Tiryakioğlu M. Review of effect of P and Sr on modification and porosity development in Al–Si alloys. Materials Science and Technology. 2010;**26**(3):262-268. DOI: 10.1179/174328409X425227

[15] SkatTiedje N, Taylor JA, Easton MA. A new multi-zone model for porosity distribution in Al–Si alloy castings. Acta Materialia. 2013;**61**:3037-3049

[16] Miresmaeili SM, Shabestari SG, Boutorabi SMA. Effect of Melt Filtration on Porosity Formation in Sr-modified A356 Aluminum Alloy. International Journal of Cast Metals Research. 2003;**16**:541-548

[17] Miresmaeili SM, Shabestari SG, Boutorabi SMA. The Effect of Sr-modification Treatment on

Porosity Formation of Reduced Pressure 319 Al-alloy Castings. Canadian Metallurgical Quarterly. 2003;**42**:245-252

[18] Shabestari SG, Miresmaeili SM, Boutorabi SMA. Effects of Sr-modification and Melt Cleanliness on Melt Hydrogen Absorption of 319 Aluminum Alloy. Journal of Materials Science. 2003;**38**:1901-1907

[19] Taylor JA, Schaffer GB, StJohn DH. The role of iron in the formation of porosity in Al-Si-Cu-based casting alloys: Part I. Initial experimental observations. Metallurgical and Materials Transactions. 1999;**30**:1643-1650

[20] Khalifa W, Samuel AM, Samuel FH, Doty HW, Valtierra S. Metallographic observations of β-AlFeSi phase and its role in porosity formation in Al-7%Si alloys. International Journal of Cast Metals Research. 2006;**19**(3):156-166

[21] Samuel AM, Doty HW, Valtierra S, Samuel FH. Beta Al5FeSi phase platelets-porosity formation relationship in A319.2 type alloys. International Journal of Metalcasting. 2018;**12**(1):55-70

[22] Samuel AM, Doty HW, Valtierra S, Samuel FH. Influence of Oxides on Porosity Formation in Sr-Treated Alloys. International Journal of Metalcasting. 2017;**11**(4):729-742

[23] A.M. Samuel, F.H. Samuel, H.W. Doty and S. Valtierra, Porosity formation in Al-Si sand mold castings, International Journal of Metalcasting, Vol. 11(4), 2017, p pp. 812-822.

[24] Elsebaie O, Samuel AM, Doty HW, Valtierra S, Samuel FH. On the Impact Properties and Fractography of Al–11%Si Casting Alloy. International Journal of Metalcasting. 2018;**12**(1):36-54

[25] Qiu D, Taylor JA, Zhang M-X, Kelly PM. A mechanism for the poisoning effect of silicon on the grain refinement of Al–Si alloys. Acta Materialia. 2007;**55**:1447-1456

[26] Nafisi S, Ghomashchi R. Grain refining of conventional and semi-solid A356 Al–Si alloy. Journal of Materials Processing Technology. 2006;**174**:371-383

[27] J. Campbell, The Solidification of Metals, Iron and Steel Institute, Publication 110, London, 1967, p. 18.

[28] Liu L, Mohamed AMA, Samuel AM, Samuel FH, Doty HW, Valtierra S. Precipitation of β-Al5FeSi phase platelets in Al-Si based casting alloys. Metallurgical and Materials Transactions A. 2009;**40**(10):2457-2469

[29] Mohanty PS, Samuel FH, Gruzleski JE. Experimental study on pore nucleation by inclusions in aluminum castings. AFS Transactions. 1995;**103**:555-564

[30] Samuel AM, Doty HW, Valtierra S, Samuel FH. Beta Al5FeSi phase platelets-porosity formation relationship in A319.2 type alloys. International Journal of Metalcasting. 2018;**12**(1):55-70

[31] L. Liu, A.M. Samuel, F.H. Samuel, H.W. Doty and S. Valtierra, Influence of oxides on porosity formation in Sr-treated Al-Si casting alloys, *Journal of Materials Science,* Vol. 38(6), 2003, pp. 1255-1267.

[32] Argo D, Gruzleski JE. Porosity in Modified Aluminum Alloy Castings. AFS Transactions. 1988;**96**:65-74

[33] J, A. Taylor, Metal related castability effects in aluminum foundry alloys, Cast Metals, Vol. 8(4), 1995, pp. 225-252.

[34] J.A. Taylor, G.B Schaffer, J. D.H. StJohn, The role of iron in the formation

of porosity in Al-SiCu-based casting alloys (Parts 1-3), *Metallurgical and Materials Transactions A*, Vol. 30A(6), pp. 1643-1650 (part 1), pp. 1651-1655 (part 2), pp. 1657-1662 (part 3), 1999.

[35] Otte M, McDonald S, Taylor J, StJohn D, Schneider W. Controlling porosity-related casting rejects: understanding the role of iron in Al-Si alloys. AFS Transactions. 1999;**107**:471-478

[36] C.M. Dinnis, J.M. Taylor, A.K. Dahle, D.H. StJohn, The role of manganese and iron in porosity formation in aluminium-silicon foundry alloys, *Light Metals 2003, Proceedings 42nd Annual Conference of Metallurgists of CIM*, pp. 483-497,Vancouver, Canada, 2003.